A Near-Real-Time Approach for Monitoring Forest Disturbance Using Landsat Time Series: Stochastic Continuous Change Detection

Su Ye*[1], John Rogan[1], Zhe Zhu[2], J. Ronald Eastman[3]

Abstract

Forest disturbances greatly affect the ecological functioning of natural forests. Timely information regarding extent, timing and magnitude of forest disturbance events is crucial for effective disturbance management strategies. Yet, we still lack an acute, near-real-time and high-performance remote sensing tools for monitoring abrupt and subtle forest disturbances. This study presents a new approach called 'Stochastic Continuous Change Detection (S-CCD)' using a dense Landsat data time series. S-CCD improves upon the 'COntinuous monitoring of Land Disturbance (COLD)' approach by incorporating a mathematical tool called the 'state space model', which treats trends and seasonality as stochastic processes, allowing for modeling temporal dynamics of satellite observations in a recursive way. The accuracy assessment is evaluated based on 3,782 Landsat-based disturbance reference plots (30 m) from a probability sampling distributed throughout the Conterminous United States. Validation results show that the best F1 score of S-CCD is 0.793 with 20% omission error and 21% commission error, slightly higher than that of COLD (0.789). In addition, two disturbance sites respectively associated with fire and insect disturbances are used for qualitative map-based analysis. Both quantitative and qualitative analysis indicate that S-CCD can achieve noticeably less omission errors than COLD for detecting those disturbances with subtle/gradual spectral change such as insect attack and drought stress. S-CCD enables complete real-time monitoring, and up to ~4.4 times speedup for computation. This research addresses the need for near-real-time monitoring and large-scale mapping of forest health, and offers a new approach for operationally performing change detection tasks from long-term and dense Landsat-based time series.

This preprint has been submitted to Remote Sensing of Environment for peer review

Key words: Time series analysis, Forest disturbance, State space model, Kalman filter, Landsat, Near real-time

*Corresponding author: Email remotesensingsuy@gmail.com Tele +1 508 826 4355

[1] Graduate School of Geography, Clark University, 950 Main Street, Worcester, MA 01610, USA

[2] Department of Natural Resources and the Environment, University of Connecticut, Storrs, CT 06269, USA

[3] Clark Labs, Clark University, Worcester, MA 01610, USA

1. Introduction

In the last two decades, linked to the recent elevated air temperature and prolonged drought, an increase in the occurrence and severity of forest disturbance has been documented over large parts of the globe (Dale et al., 2001; Seidl et al., 2017; Turner et al., 1998); notably, insect outbreak (Kautz et al., 2017; Paritsis and Veblen, 2011),wildfire (Pechony and Shindell, 2010; Westerling, 2016) and drought (Allen et al., 2015). Forest disturbance events directly emit carbon to the atmosphere through oxidation and decomposition of wood (Masek et al., 2008), and yield significant impacts on ecosystem services of national forests such as climate regulation and biological diversity conservation (Curran and Trigg, 2006). Therefore, it is important to systematically gather information regarding the extent, timing and magnitude of forest disturbance in an accurate and timely manner, enabling an early warning and effective management to prevent further loss of forested land (Rogan and Mietkiewicz, 2015).

For decades, satellite remote sensing has been promoted as a key data source for operational forest monitoring (Pasquarella et al., 2017). Particularly, the opening of the Landsat archive (Woodcock et al., 2008) has led to improved opportunities for characterizing forest disturbances from a long-term and consistent Landsat time series (Zhu, 2017). Compared with low-resolution datasets such as Moderate Resolution Imaging Spectroradiometer (MODIS, 250-1000 m resolution), Landsat-based time series are provided in a sufficient temporal length of 40-year global record of fine-grained observations (30 m) (Masek et al., 2013). Therefore, Landsat is often perceived as the best free-access remotely sensed data source for resolving the full range of disturbance occurrence (Cohen et al., 2017; Cohen et al., 2016; Kennedy et al., 2014; Ye et al., 2018). Recently, the release of Landsat Analysis Ready Data (ARD) has eased automation for monitoring large-scale forest disturbances (Dwyer et al., 2018). The Landsat ARD gridded all available Landsat-4 and -5 TM, Landsat-7 ETM+ and Landsat-8 OLI/TIRS to an Albers Equal Area (AEA) Conic map projection, and are consistently geo-registered and atmospherically corrected; and hence holds the highest level of scientific standards and processing required for immediate use (Zhu, 2019).

The Landsat ARD requires the minimum of user effort for data preprocessing, greatly facilitating a large-scale and long-term time series analyses (Dwyer et al., 2018).

A wealth of methodologies on satellite-based time series analysis have been developed for land cover change detection and characterization (Kennedy et al., 2010; Verbesselt et al., 2010a; Zhu and Woodcock, 2014b; Zhu et al., 2012). These algorithms are often categorized based upon their monitoring strategies: offline or online monitoring (Bullock et al., 2019; Zhu, 2017). Offline monitoring focuses on a retrospective analysis when the collection of time series data is completed, and seeks to reconstruct forest disturbance history. The representative approaches for this category include LandTrendr (Kennedy et al., 2010), DBEST (Jamali et al., 2015) and the ensemble approach (Bullock et al., 2019). Online monitoring is applied to a practical scenario that the new observations are successively collected and processed in a timely fashion, and hence can be used for near real-time monitoring. Representative approaches for online monitoring are Breaks for Additive Season and Trend Monitor (BFAST Monitor) algorithm (Verbesselt et al., 2012) and Continuous Change Detection and Classification (CCDC) (Zhu and Woodcock, 2014b; Zhu et al., 2019), though they are also applicable for offline monitoring. The BFAST was originally designed for temporal segmentation of MODIS-based time series (Verbesselt et al., 2010a), and was later modified (BFAST Monitor) to address near real-time detection for drought-related vegetation disturbance (Verbesselt et al., 2012). BFAST Monitor is a univariate approach that uses a single spectral band or index, while it has been reported that multiple bands or indices is more preferable because forest disturbance has a multi-spectral expression requiring multi-band inputs (Cohen et al., 2017; Zhu et al., 2019).

CCDC is a multivariate time-series model that uses all available Landsat 4-8 data for change characterization and land cover classification (Zhu and Woodcock, 2014b). The CCDC first applies the Fmask (Zhu and Woodcock, 2012) and Tmask algorithm (Zhu and Woodcock, 2014a) to screen clouds, cloud shadows and snow, and then build a harmonic model for each spectral band based on remaining clear observations. A breakpoint indicative of the timing of the disturbance is identified when the minimum discrepancy between actual and predicted reflectance of spectral bands for a monitoring window is greater

than a predefined change threshold (Zhu and Woodcock, 2014b). Recently, an improved algorithm called 'COntinuous Monitoring of Land Disturbance'(COLD) was developed based upon CCDC (Zhu et al., 2019). COLD introduced several improvements such as disturbance extraction, temporally-adjusted Root Mean Square Error (RMSE), change angles for disturbance confirmation (Zhu et al., 2019). An important finding for COLD is that using the highest frequency for harmonic model updates, that is per observation instead of per a time span for the CCDC, can reduce ~20% commission errors (Zhu et al., 2019). Zhu et al. (2019) tested the performance of COLD using 7,200 Landsat time series plots randomly selected across the conterminous United States, and reported that the COLD algorithm achieves a higher accuracy than CCDC, with 27% omission error and a 28% commission error for a variety of land disturbance types.

However, while the COLD algorithm has achieved improved performance for change detection accuracy, there are several issues limiting its implementation for operational monitoring. First, COLD is computationally expensive, which takes ~5000 computing hours for a Landsat ARD time series (Zhu et al., 2019). The high computational requirement imposes limits on the application of COLD for a wide range of scientific research, especially for a large-area mapping such as at a state or continental scale. The cause for the slow speed is mainly from the per observation updating approach (Zhu et al., 2019). For example, if the time series of a single pixel has 500 clear observations, COLD needs to re-train the model using the 'Least Absolute Shrinkage and Selection Operator' (LASSO) algorithm for approximately 500 times to complete a detection for this pixel. Computational redundancies arise from reconstructing models from scratch for each new observation being added to the time series. Second, the former version of COLD, namely CCDC, was designed to detect land cover change, and is less helpful for detecting those disturbances that yield small to medium spectral change magnitude (Brown et al., 2019; Cohen et al., 2017; Zhu et al., 2019). A possible reason provided is that CCDC identifies gradual changes as the slope in the harmonic regression model as opposed to attributing them to a change on a specific date. Though this issue was alleviated by COLD, it has not been fully solved yet because COLD reported only 60% producer accuracy for the disturbance category 'stress' (Zhu et al., 2019). Third, within the current workflow of COLD, near real-

time monitoring is not fully operational because: 1) COLD is a memory-intensive algorithm which requires loading all images to update model coefficients and to calculate temporally-adjusted RMSE for each new observation; 2) a certain steps of COLD such as minimum RMSE require an input of a complete time series, which does not satisfy the need of near real-time monitoring.

In this study, we describe a new algorithm called 'Stochastic Continuous Change Detection' (S-CCD) that is developed to detect forest disturbance from Landsat time series in a recursive fashion. S-CCD introduces the state space theory into the current framework of COLD, aiming to address three objectives: 1) to enhance detection accuracy, especially for those forest change with small spectral change magnitudes while keeping a low rate for commission errors; and 2) to provide an operational framework for near real-time monitoring; 3) to improve computational efficiency, enabling a long-term time series analysis for a large-area forest disturbance characterization.

In what follows, we first provide an intuitive explanation for state space models and the Kalman filter as the mathematical foundation of S-CCD (Section 2), describe our S-CCD algorithm focusing on different steps with COLD (Section 3), introduce our reference dataset and validation metrics (Section 4) and exhibit the results for both quantitative and qualitative evaluation (Section 5), and finally discuss advantages and future work for S-CCD (Section 6). Of particular note is that Section 5.3 presents a high-performance software package for both S-CCD and COLD implemented in C language.

2. State space model and the Kalman filter

The new approach built upon the State Space Model (SSM), an established time-series mathematical framework that allows for modeling a dynamic of observed measurements as being explained by a vector of latent state variables. The SSM has two foundational 'stochastic' assumptions: 1) observations are formulated as a sum of a stochastic item linked to the uncertainty within the data themselves, namely 'observational noise' (ϵ_t), and a vector of latent variables called 'states' (α_t); 2) states which are evolving over time as a stochastic process with being affected by a 'process noise' (η_t). Different from classical

decomposition models such as harmonic regression used in BFAST and CCDC, SSM allows for trend and cycle components to be evolving randomly rather than deterministically (see Fig. 1), hence we called it as 'Stochastic Continuous Change Detection'.

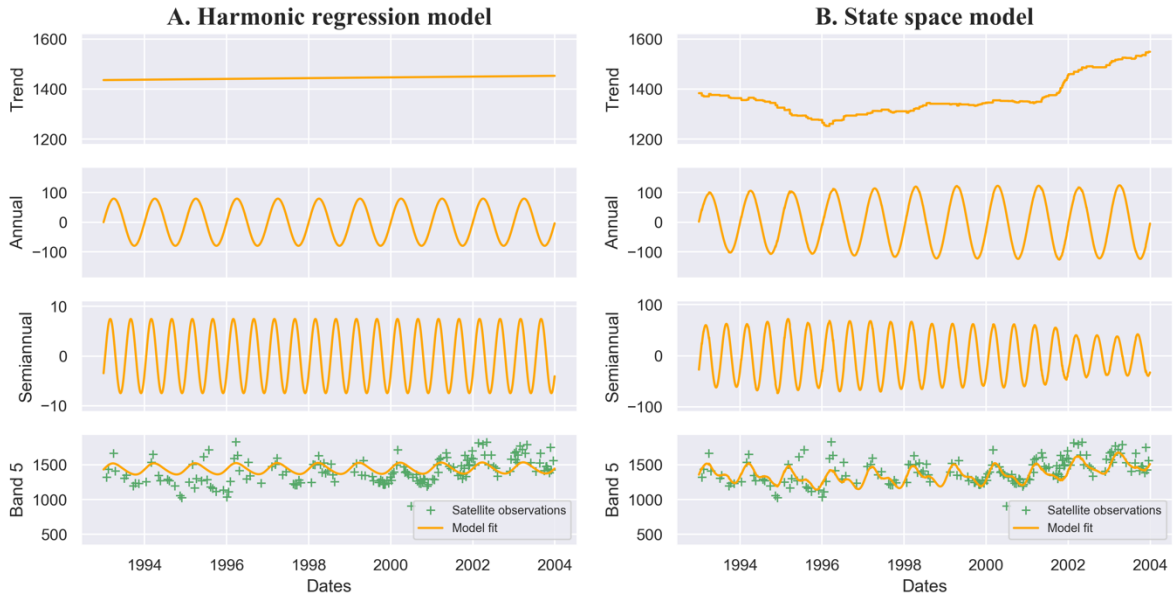

Fig. 1. The comparison between a harmonic regression model (A) and a state space model (B) for fitting curves. The harmonic regression model has a rigidity for consistent coefficients such as intercepts, slope and Fourier coefficients, while the state space model assumes that each component is evolving as a stochastic process and yields the optimal estimate for each time step based upon its state covariance and observational noise, so that the model coefficients vary over time.

The general Gaussian SSM can be written in the form as below (Durbin and Koopman, 2012):

Observation equation: $y_t = Z\, a_t + \epsilon_t,\ \epsilon_t \sim \mathrm{N}(0, \mathrm{H})$ (1)

State equation: $a_{t+1} = T a_t + \eta_t,\ \eta_t \sim \mathrm{N}(0, \mathrm{Q})$ (2)

Where y_t is the observation at time t, ϵ_t and η_t are two mutually independent random variables that follow a normal distribution with mean 0 and variance H, and variance Q, respectively. Z is a system matrix in a binary form, which indicates those state items that directly contributes to the observation. T is a transformation matrix defining how a state vector evolves over time (mathematical definitions for Q, Z and T are detailed in the appendix). State space representation is central to statistical treatment of structural time

series models, owing to its ability of allowing for structural components to be modeled explicitly by state variables (Brockwell and Davis, 2013; Durbin and Koopman, 2012). SSM holds great promise for processing remote sensing time series, which are well known for the structure of 'trend + cycles' (Eastman et al., 2013; Verbesselt et al., 2010b; Zhu and Woodcock, 2014b).

The SSM for the state of 'trend' is formulated as a random-walk model:

$$\mu_{t+1} = \mu_t + \xi,\ \xi \sim \mathrm{N}(0, \sigma_\xi^2) \tag{3}$$

Where ξ is a process noise item for the trend. The 'cycle' process requires two state variables to define:

$$c_{t+1} = c_t\, cos\, \lambda_c\ +\ c_t^*\, sin\, \lambda_c\ +\ \omega_t,\ \omega_t \sim \mathrm{N}(0, \sigma_\omega^2) \tag{4}$$

$$c_{t+1}^* = -c_t\, sin\, \lambda_c\ +\ c_t^*\, cos\, \lambda_c\ +\ \omega_t^*,\ \omega_t^* \sim \mathrm{N}(0, \sigma_{\omega^*}^2) \tag{5}$$

Where λ_c is the frequency of the cycle, ω_t and ω_t^* are independent noise items. c_t is the primary cycle state, while c_{t+1}^* is an accessory state variable that is not included for prediction of y_t and only used to enable a recursive form of mathematical computation (so its corresponding element in Z is 0). For a classic model for 'trend + annual cycle + semi-annual cycle', the state vector can therefore be given by

$$a_t\ =\ (\mu_t,\ c_{t,annual},\ c_{t,annual}^*,\ c_{t,semi},\ c_{t,semi}^*)' \tag{6}$$

Compared with 6-coefficients harmonic model, our state space model has no component corresponding to 'slope', because S-CCD is essentially a Markov model forecasting present states based on only the last observation, not all historical observations (i.e. decreasing or increasing trend). The advantages for eliminating 'slope' component will be discussed in Section 6.

The Kalman filter is the most common tool providing an operational treatment for SSM. The Kalman filter was first developed for estimating real-time trajectory of the spacecraft for the Apollo program (Schmidt, 1981), and was later introduced to other application domains such as the control of linear systems (Davis and Vinter, 1985) and econometric modeling (Pasricha, 2006). Recently, the Kalman filter was applied to improve satellite-based time series analysis for applications such as crop phenology estimation (Vicente-

Guijalba et al., 2014), synthetic NDVI image generation (Sedano et al., 2014) and near real-time monitoring of defoliation (Olsson et al., 2016). The Kalman filter is claimed to produce an optimal estimate in the sense that it always reaches the minimum mean square error, and is capable of predicting measurements in a recursive manner so that new measurements can be processed as they arrive (Durbin and Koopman, 2012; Kalman, 1960). As such, the Kalman filter has great potential for being a fundamental tool of satellite-based near real-time monitoring.

Fig. 2 presents an intuitive explanation of a Kalman filter for adjusting its modelling curve successively once a new observation is available. The Kalman Filter defines one-ahead-step prediction for the date t as

$$\widehat{y_t} = a_t * Z \quad (7)$$

When a new observation, '2000-12-27', is introduced into the time series, there is a discrepancy between the one-ahead-step prediction (the solid orange dot) and the new observation (the green cross) called 'innovation'. In a Kalman filter, the 'innovation' can be divided into two components: 1) observational noise; and 2) model updates brought by the new observation. The Kalman gain is the relative weight assigned to actual model updates, which can be estimated by covariances of states and observational noise. Once the Kalman gain is computed, the Kalman filter can filter out observational noise from the innovation. The new model coefficient will be adjusted based upon the remaining part that is considered only associated with actual model updates, yielding a new fitting curve 'filtered state' (the blue dot). The filtered states (or adjusted coefficients) will then be used to predict the next observation (the dashed orange line).

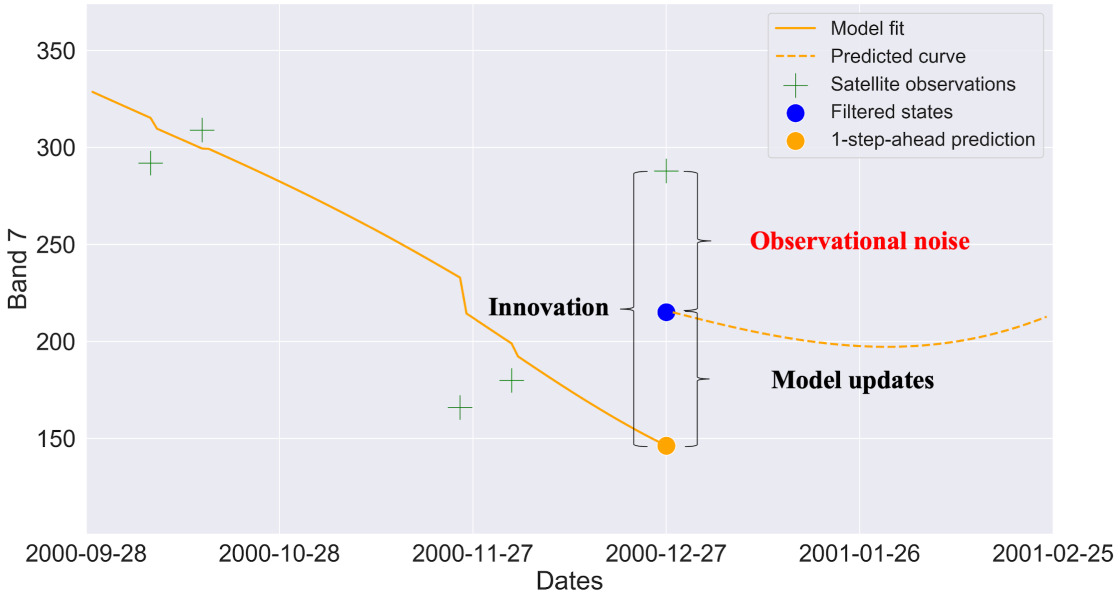

Fig. 2. An intuitive explanation of Kalman filter for a Landsat time series. When a new observation at the date of '2000-12-27' is introduced to the system, the Kalman filter measures the difference between the actual observation (the green cross at '2000-12-27') and the predicted value (the green dot), namely 'innovation'. The fitting curve for the model will be adjusted to align with the optimal estimate for the current states (the 'blue dot') by filtering out 'observational noise' from 'innovation'.

Vegetation dynamics often exhibit a complex trend, which is not guaranteed to be adequately approximated by a single linear mode (Burkett et al., 2005; Zhao et al., 2019). The assumption for stochastically varying states for SSM and Kalman filters avoids the rigidity of classical decomposition that assumes the stationarity of linearity and seasonality, hence complex dynamics from time-series data are uncovered and more local fluctuations can be captured (Brockwell and Davis, 2013). The flexibility of dynamic modeling directly leads to better fitness of the model, and hence potentially increases the sensitivity of the model to subtle changes because change magnitudes are often calculated relative to measurement of model fitness such as Root Mean Square Error (RMSE). Other advantages of a state space analysis for satellite-based time series include: 1) simple mathematical treatment of missing data (shown in Appendix) which is critical for dealing with satellite-based time series known for its temporal irregularity; 2) explicit consideration for

measurement uncertainties for the noisy nature of remote sensing data; 3) high computational efficiency due to its recursive form.

3. Method

Fig. 3 presents the workflow of S-CCD. S-CCD consisted of three primary stages: data preparation, model initialization and continuous monitoring. We used five spectral bands of surface reflectance products (green, red, NIR, SWIR1 and SWIR2) as the algorithm inputs because Zhu et al. (2019) have shown that these five spectral inputs alone can achieve the best performance compared with being combined with vegetation indices. We applied the same steps as COLD for S-CCD for data preparation, for which we refer to Section 3.1.1 of (Zhu et al., 2019).

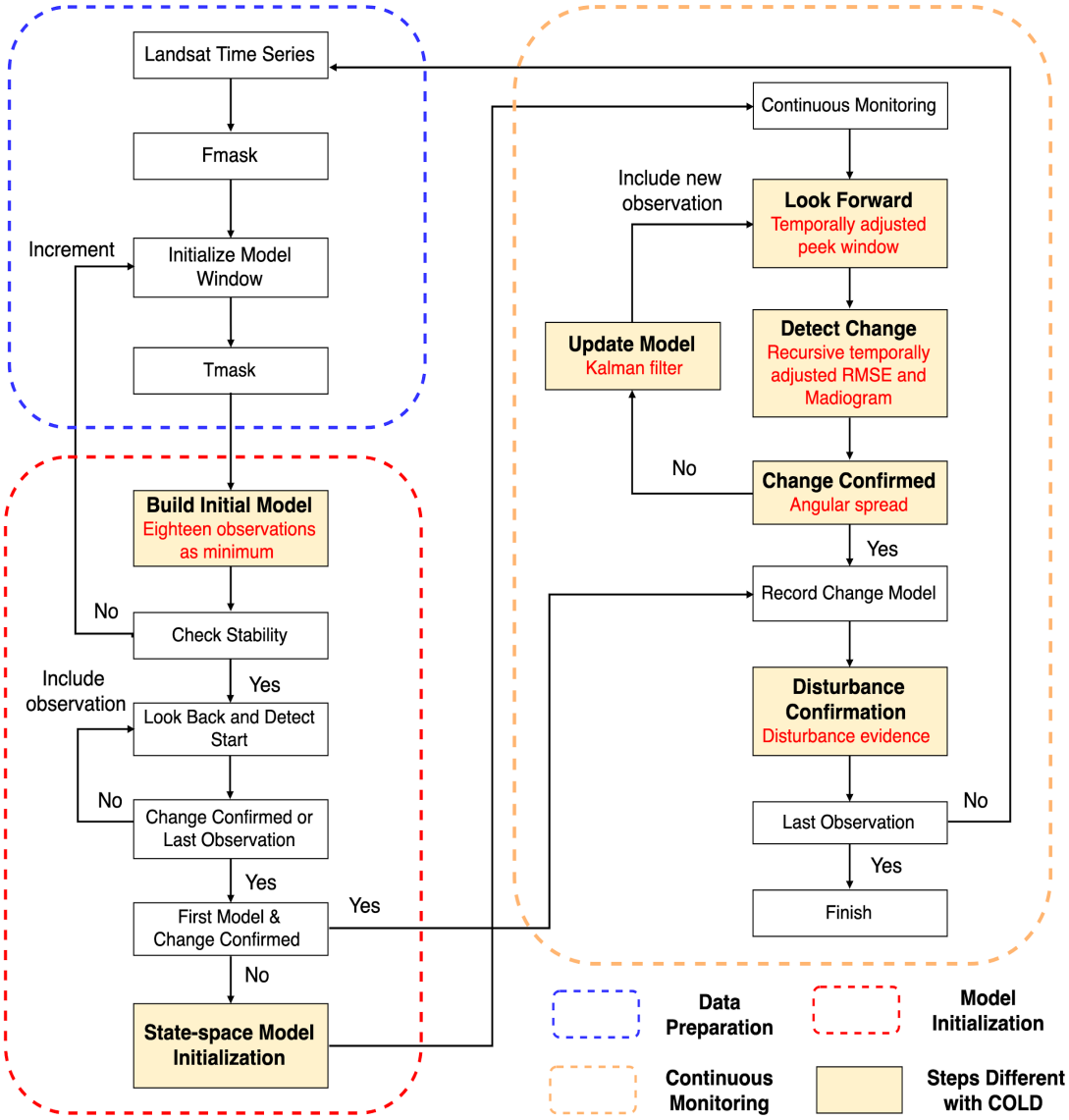

Fig. 3. The workflow of the proposed Stochastic Continuous Change Detection (S-CCD). Same as the original COntinuous monitoring of Land Disturbance (COLD), the workflow consists of three stages: 1) data preparation; 2) model initialization; 3) continuous monitoring. The different steps between S-CCD and COLD are highlighted as yellow polygons.

3.1 Build Initial Model

After a clear time series is prepared by Fmask (Zhu and Woodcock, 2012), initialization model window and Tmask (Zhu and Woodcock, 2014a), S-CCD needs to seek a stable stage to define a statistical reference for change identification which adopts the stability test and 'looking back' procedure (Zhu et al., 2019).

The subtle modification for S-CCD is that we used 18 instead of 12 as the required minimum number of clear observations for an initialization window: our new approach assumes a fixed structure of 'trend + annual + semiannual' for a time series which can be equivalent to 6-coefficients harmonic model. The suggested minimum observation window for a LASSO regression is 'number of coefficients * 3', hence the minimum observation number is set as 18. The reason for excluding a trimodal component (8-coefficient model) is discussed in Section 6.

3.2 State space model (SSM) initialization

In S-CCD, an additional step is to initialize the parameters and the structural elements for state space models before the continuous monitoring starts. The initial SSM parameters include observational noise (H), process noise (Q), initial states (a_0) and initial covariance (P_0).

The parameters H and Q are the two most important SSM parameters, representing the uncertainty level for observations and each stochastic process. They are often estimated by maximizing likelihood through a Quasi-Newton numerical searching algorithm in literature (Durbin and Koopman, 2012; Helske, 2016). However, after initial tests, we learned that the Quasi-Newton algorithm was extremely inefficient for processing millions of pixel-based time series. To overcome the issue, we designed a fast method for estimating H and Q. We set the observation noise as the squared RMSE of LASSO regression for the initialization window: $H = RMSE * RMSE$. To estimate Q, the Kalman filter with the initial process noise $Q_{ini} = diag(0,0,0,0,0)$ is first applied to estimate filtered states for each observation within the initialization window. Then, the process noise is corrected using the results of estimated filtered state from the first run: the filtered trend state is ideally consistent if there is no process noise, and thereby, a single process noise can be estimated as:

$$\xi_n = (\mu_{t(n)|t(n)} - \mu_{t(n-1)|t(n-1)}) \,/\, sqrt(t(n) - t(n-1)) \quad (8)$$

Where $t(n-1)$ and $t(n)$ is the date for two temporally neighboring observations, namely t-1 th and tth observation, $\mu_{t(n-1)|t(n-1)}$ and $\mu_{t(n)|t(n)}$represents filtered trend states for these two observations.

The process noise for the trend state can be calculated as $\sigma_{\xi}^{2} = var(\xi_n)$. The process noises for components are viewed as being proportional to the mean of the absolute value of the corresponding states, so the seasonal process noise can be calculated as:

$$\sigma_{\omega}^{2} = \frac{\sum_{n=1}^{N}|c_{t(n)}|}{\sum_{n=1}^{N}|\mu_{t(n)}|}\,\sigma_{\xi}^{2} \quad (9)$$

Initial states a_0 are estimated from using 6-coefficient LASSO regression to fit all observations within an initialization window. Initial covariance P_0 represents the uncertainty level of a_0. P_0 is often assumed to be the isotropic matrix, $P_0 = \lambda \mathrm{I}$. The literature indicates that the uncertainty of Landsat surface reflectance product is under the surface reflectance (SR) specification, defined as 5% × SR + 0.005 (Claverie et al., 2015; Ju et al., 2012). Accordingly, we used 5% for estimating uncertainties of initial states, that is $\lambda = (Z\ \alpha_t\ *\ 5\%)^2 / sum(Z)$.

3.3 Temporally adjusted peek window

For each newly-collected clear observation, S-CCD compares predictions from the Kalman filter and actual observations based upon a number of consecutive anomaly observations, called the 'peek window' for CCDC-like approaches (Davis et al., 2017). COLD approach determines the number of consecutive observations via calculating the median revisit days across the entire time series. If the median revisit days are shorter than normal Landsat temporal density (16 days), more consecutive observations need to be included, and the probability threshold that all observations need to exceed is decreased to compensate (Zhu et al., 2019). This approach requires an entire time series to compute median revisit days. We developed a completely online approach for adjusting the peek window for S-CCD. The number of observations for an temporally-adjusted peek window is defined as the minimum number satisfying 1) minimum requirements for consecutive observations, i.e., $conse_{def}$; and 2) the minimum peek days (min_peek_days):

$$conse_{def} = min\{x |\ x \geq conse_{def}\ and\ span(x) \geq min\_peek\_days\} \quad (10)$$

The defaulted consecutive number $conse_{def} = 6$. The min_peek_days is related to the temporal span indicating consistency of a disturbance event affecting vegetation. If min_peek_days is set to be too long, signals of a disturbance might be diluted due to post-disturbance forest regrowth; if too short, some ephemeral changes such as soil moisture change might be misidentified as disturbance. As the normal Landsat density is 16 days per clear observation (Zhu et al., 2019), the normal peek window width for min_peek_days is 6 * 16 = 96 days. We explored the algorithm performance by using several min_peek_daysbelow the normal peek window width (e.g. 60, 70, 80 days). Choosing min_peek_daysas 80 days shows the best result (see S1 in the supplementary material). The threshold probability is also adjusted when a peek window chooses a consecutive observation number larger than $conse_{def}$, following Equation S4 in (Zhu et al., 2019).

Another advantage of the new peek window in terms of COLD approach is making it feasible to account for variability in Landsat observation frequency across not just space, but also time. The new definition of the peek window considers that the consecutive number is not fixed for a single time series. Time series segments collected in the early days (e.g. before the launch of Landsat 7 ETM+ on 1999) often have a lower temporal density than the most recent collections. Large changes in frequency driven by the number of active sensors aboard Landsat satellites had an influence on the CCDC/COLD change detection records (Brown et al., 2019): higher detection rates often occur at higher observation frequency, including commission errors brought by ephemeral forest change. The new peek window enables an adjustment of consecutive observations based upon the local temporal density for the peek window, because it defines the peek window according to the physical attribute of a disturbance signal, namely lasting days, not satellite observation count.

3.4 Recursive temporally-adjusted RMSE

Squared differences between predictions and observations is used to evaluate deviation of the current peek window from the ‘stable stage’. RMSE is used to normalize the square difference, which is critical for

decisions on the occurrence of breakpoints. Considering that RMSE often exhibits a yearly pattern over the whole time series (Zhu et al., 2015), the COLD algorithm employs a temporally-adjusted RMSE that is calculated based on the temporally closest 24 observations to the peek window. For operational near real-time monitoring, this temporally-adjusted RMSE needs to be re-computed by loading all images back into the model for a new observation with its date. We designed a novel recursive method based upon two histograms respectively for clear observation counts (Fig. 4A) and square of RMSE (Fig. 4B) for Days of Year (DOY), which eliminates the need for processing all images for each new observation. Both histograms are defined as a bin width of 6 days, and 61 bins in total. The two histograms keep updating when a new observation is available. To compute a temporally-adjust RMSE for a new observation, S-CCD will start from the bin at the middle date of the peek window ('Step 1' in Fig. 4A), and expand the RMSE window by an increment of one bin on the left and the right side each time, until the RMSE window include $\geq$ 24 observations ('Step 3' in Fig. 4A). The temporal RMSE is computed as the average RMSE*RMSE based on the sum of RMSE*RMSE and the total count within the resultant RMSE window.

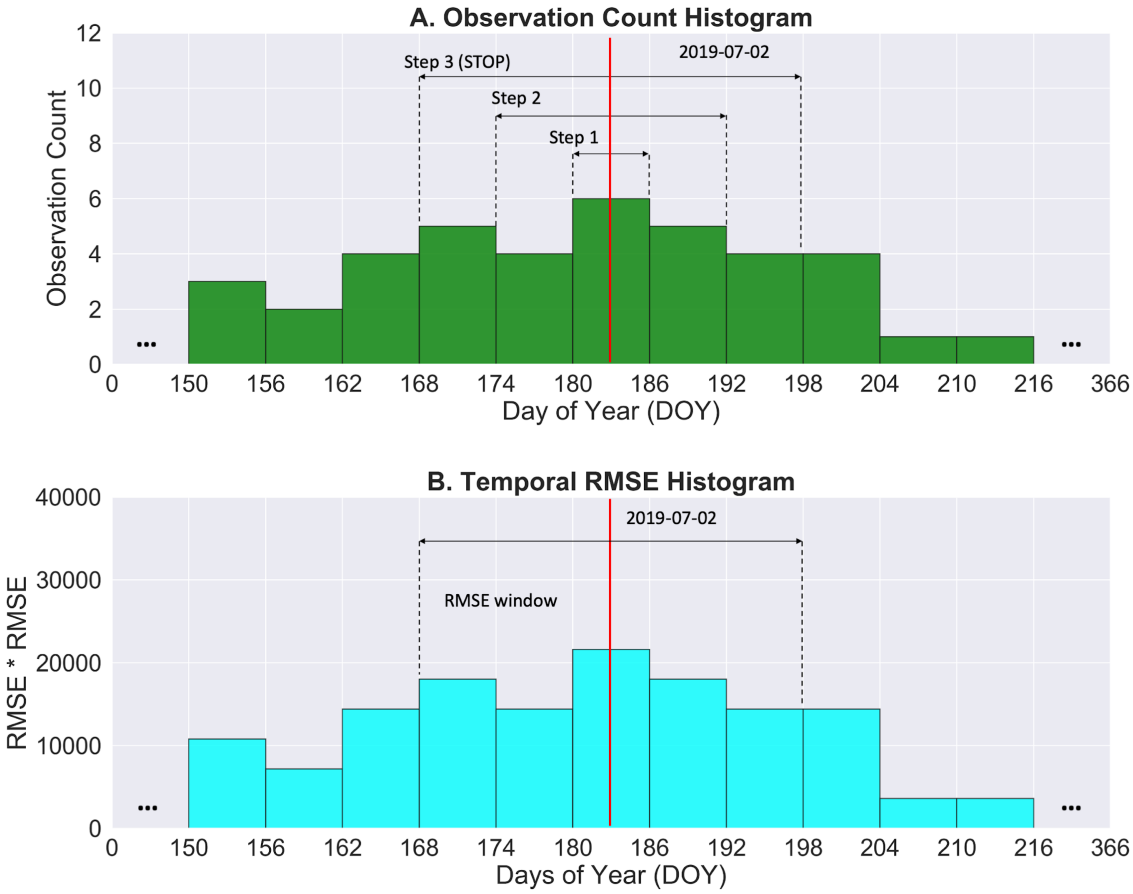

Fig. 4. The explanation for a recursive calculation of temporal RMSE: the algorithm searches a RMSE window that just covers ≥ *24* observations by an increment of a bin on both sides in an observational count histogram (Fig. 4A). Once it stops (Step3 in Fig. 4A), the temporal RMSE is computed as the average RMSE*RMSE within the resulting RMSE window.

Likewise, to enable near real-time monitoring, we used a dynamic minimum RMSE (or temporal lag-1 madogram), instead of a static minimum RMSE used in (Zhu et al., 2019), to define the minimum value of RMSE for each band: the madogram is updated each year using all clear past observations.

Therefore, the new RMSE for S-CCD is computed as

$$RMSE_i = max(\sqrt{\frac{\sum_{\in\varphi} RMSE_{i,b} * RMSE_{i,b}}{\sum_{\in\varphi} count_{i,b}}},\ dynamic\_\min\_RMSE_i) \quad (11)$$

Where φ is a group of all bins (b) within the resultant $RMSE$ window, and i is ith Landsat band.

We define the Standardized Change Vector (SCV_n) as a vector of the difference between a multispectral observation n at time $t(n)$ and its one-step-ahead prediction relative to $RMSE$:

$$SCV_n = \left[\frac{y_{t(n),1} - \hat{y}_{t(n),1}}{RMSE_1}, \frac{y_{t(n),2} - \hat{y}_{t(n),2}}{RMSE_2}, \dots \frac{y_{t(n),B} - \hat{y}_{t(n),B}}{RMSE_B}\right] \quad (12)$$

B is the number of bands used, i.e., 5 (green, red, NIR, SWIR1 and SWIR2). Similar to the COLD algorithm, we used the minimum change magnitude for each change vector within the peek window to detect the breakpoint. The minimum change magnitude (MCM) is used as the indicator of breakpoints, which is calculated as the minimum norm of SCV_n for a peek window. MCM follows the Chi-squared distribution with k degree of freedom (Zhu et al., 2019), where k is the number of the used spectral bands, namely '5'. A breakpoint candidate is identified if it meets the condition, where p refers to the current peek window:

$$MCM = \{\|SCV_n\|^2\} \sim \chi^2(k) > \chi^2_{threshold}(5) \quad (13)$$

3.5 Confirm change using angular spread

Ephemeral and systematic noise may also lead to relatively large change magnitudes for all observations within a peek window. The disturbance signal, however, should have a consistent change direction for multispectral surface reflectance bands. Therefore, the time series model needs to confirm the change from the consistency of change angles once the Chi-squared distribution test is passed. COLD confirms breaks using the mean included angle between pairs of neighboring change vectors smaller than 45 degrees. We found that this strategy is sensitive to outliers: for example, if there is an outlier in the six consecutive observations, two out of five neighbor pairs will be affected by this outlier (40% of the candidate angles); if there are two outliers in a peek window, more than half of neighbor pairs are biased. We designed a new change angle index called 'angular spread', referred as the angle between the standardized change vector for nth observation (SCV_n) and the median standardized change vector ($MedSCV$) (see Fig. 5). The mediam change vector of a peek window here is used to represent the average of the spectral response of a disturbance. The observations for a disturbance should concentrate around the median change vector in an

ideal condition. We define 'Mean Angular Spread' for a peek window (Equation 14) to represent the average angular departure of each candidate change vector to medium change vector. We compared the performance of the maximum mean included angle as 45 degrees (the COLD approach) and the maximum angular spread with 30, 45 degree. The best result is achieved by using angular spread as 30 degrees (Fig. S2 in the supplementary material). The advantage of using 'Mean Angular Spread' is that is less sensitive to outliers existing in a peek window. For example, an outlier only affects a single change angle out of six angles for a default peek window (16.7% of the candidate angles).

$$Mean\ Angular\ Spread\ = \frac{1}{conse_{adj}} \sum_{n=1}^{conse_{adj}} \theta_{(SCV_n,\ MedSCV)} < 30^{\circ} \quad (14)$$

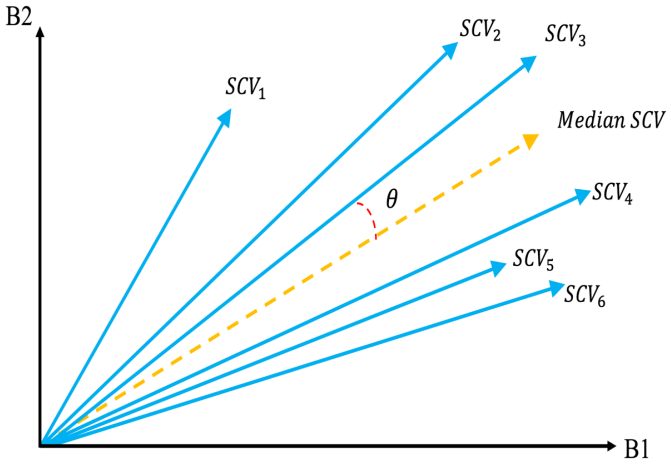

Fig. 5. The explanation of 'angular spread' for a peek window consisted of 6 consecutive observations with two spectral bands ($B1$, $B2$). Angular spread is computed as the mean angle for θ, which is the included angle between the Standardized Change Vector ($SCV_1, \ldots, SCV_6$) and the Median Standardized Change Vector ($Medium\ SCV$).

3.6 Update model using the Kalman filter

For those observations that are identified as being unchanged, non-consecutive outlier removal will be used with a change probability of 0.99999 (same as Zhu et al. (2019)). If the observation passes the outlier test, it will be inputted to the system to update the model using the Kalman filter (see the Appendix). Instead of

rebuilding LASSO regression each time, the Kalman filter has an extremely simple mathematical treatment for updating models.

3.7 Disturbance identification

Breakpoints detected by the above procedure are not necessarily associated with forest disturbance, but maybe forest recovery. As the final step, we need to single out those breaks that are related to forest health decline led by disturbance. A typical forest disturbance will cause lower NIR, higher Red and higher SWIR values. Such spectral change, however, might be asynchronous. For example, when a forest is attacked by mountain pine beetle, the increase of SWIR often occurs first due to increased water stress, then is increasing red band, and finally the NIR band decreases owing to needle drop. Hence, we created an index called '*disturbance evidence*' (see Equation 15) based on the medium Standardized Change Vector ($MedSCV$) associated with detected breakpoints. '*Disturbance evidence*' aims to provide a combined analysis for multiple bands instead of a single band index. The breaks that are identified as being disturbance-related need to have a disturbance evidence larger than zero:

$$Disturbance\ evidence = MedSCV_{RED} - MedSCV_{NIR} + MedSCV_{SWIR1} > 0 \quad (15)$$

We compared '*Disturbance Evidence*' with COLD disturbance extraction with thresholds 0, -0.01, -0.02, and -0.03. '*Disturbance Evidence*' had a higher best F1 score better than all other COLD disturbance extraction methods at all five thresholds (see Fig. S3 in the supplementary material).

4. Study area, data and accuracy assessment

Our accuracy assessment is consisted of a quantitative (plot-based) analysis against a comprehensive forest disturbance dataset, and qualitative (map-based) evaluation over two disturbance sites. For the quantitative accuracy assessment, a benchmark forest disturbance database (Cohen et al., 2016; Zhu et al., 2019) is chosen that includes 3,503 Landsat-based forest plots across the conterminous United States (US) with well-interpreted disturbance timing and types. The plots were sampled by a two-stage stratified cluster design (Cohen et al., 2016). A stratified sampling was first applied to select 180 Thiessen Scene Areas

(TSAs; (Kennedy et al., 2010)) out of 420 TSAs divided into Mountain West, Lowland West, Central, Northeast and Southeast US ecoregions as strata. For the second stage of sampling, 7,200 initial Landsat plots were randomly chosen with a sample of 40 Landsat plots for each TSA, and then those plots with the primary type of its land cover type was 'forest' at any time during the period of 1984-2012 were selected, following the procedure of Cohen et al. (2016). Further, reference plots that do not satisfy the criteria of enough clear sky observations (at least 24), have large data gaps (more than three years without any observations), or have a disturbance with an interval of longer than 10 year, or difficult to interpret were excluded (Zhu et al., 2019). As a result, a total of 3,782 forest plots across the conterminous US were identified as our reference samples.

For the Landsat plots, forest disturbance occurrence between 1984 and 2012 were interpreted by USDA Forest Service by combining plot-based time series visualization and high resolution Google Earth images (Cohen et al., 2016); these samples were checked and corrected by five interpreters by eliminating the disturbance plots that were not visually confirmed from the Landsat time series (Zhu et al., 2019). Causal agent class of disturbances were interpreted with the aid of high-resolution Google Earth imagery, and an ancillary database from multiple government agencies such as U.S. Forest Service Aerial Detection Surveying maps [4], Natural Resource Manager (NRM) database [5], etc (Zhu et al., 2019). As a result, 3,782 forest plots were separated into 2,704 undisturbed plots and 1,078 disturbed plots, which have 1,413 disturbance occurrences in total (some plots have successive disturbance occurrences such as fire and timber harvest). Among these disturbance occurrence, the most causal agent of disturbances is harvest (n = 903), followed by mechanical (n = 149), stress (n = 141), fire (n = 127), and others (n = 83, e.g., hydrology, wind, debris, land use change). For a detailed description of these disturbance causal agent classes, we refer to (Cohen et al., 2016). The spatial distribution of 3,782 Landsat plots labeled as undisturbed or the number of disturbance occurrences is shown in Fig. 6. We randomly selected 50% of the reference samples (1,891

[4] http://www.foresthealth.fs.usda.gov/portal/Flex/IDS
[5] https://www.fs.fed.us/nrm/index.shtml

Landsat plots) for algorithm development and parameter calibration. The other 50% of the reference samples were used as a holdout validation set to evaluate the comparative performance of S-CCD and COLD.

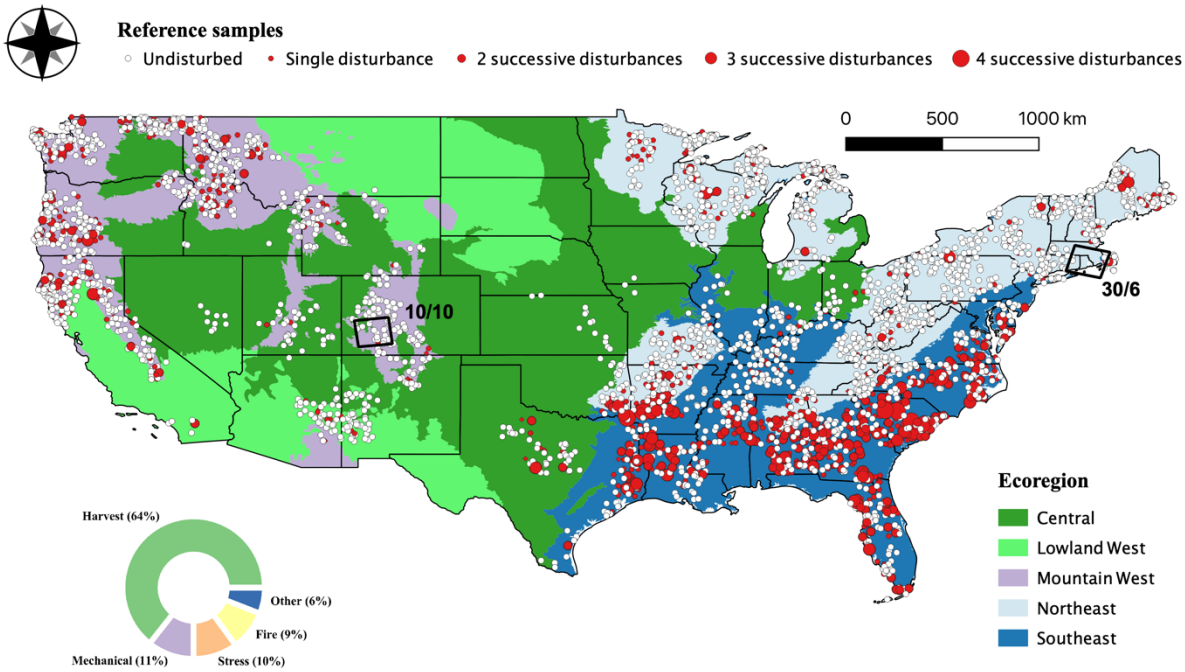

Fig. 6: the spatial distribution of 3,782 reference sites, and two Landsat ARD scenes chosen as the study areas. The reference sites include 2,704 undisturbed plots ('white circles') and 1,078 disturbed plots (red circles), which were collected using a stratified sampling based on the ecoregions across the United States. There are 1,413 disturbance occurrences in total, and the disturbance categories were dominated by the disturbance category 'Harvest' (63.9%), followed by 'Mechanical' (10.5%) and 'Stress' (9.9%). Landsat ARD 10/10 is located in the south Colorado including a region where Papoose fire happened in 2013; Landsat ARD 30/6 is located in the New England, including a site affected by gypsy moth infestation in 2016 and 2017.

Considering that different algorithms may have different sensitivities to disturbance magnitudes based on change probability thresholds, the omission and commission rates based on a series of change probability, namely 0.90, 0.925, 0.95, 0.975, 0.99, were chosen for accuracy assessment. The overall performance is evaluated using the F1 score, because it provides a balanced assessment for omission and commission rates. The definition of omission, commission rates and F1 score are the same as Zhu et al. (2019).

$$F1\ score = \frac{(1-commission)*(1-omission)}{2-commission-omission} \quad (16)$$

In addition to quantitative accuracy assessment, qualitative map-based comparisons are performed by evaluating break year maps detected by two algorithms. We chose two Landsat ARD tiles that were respectively affected by fire and insect disturbance. The fire site sits at the San Juan and Rio Grande National Forests in southwestern Colorado, where the second largest fire in Colorado history, West Fork Fire Complex, burned 438 square kilometers of forested in June and July 2013 (Verdin et al., 2013). The burned area was dominated by Engelmann spruce (*Picea engelmannii*) and Subalpine fir (*Abies lasiocarpa*) (Carlson et al., 2017), and the burn severity was moderate or high for 59 percent of the area within the burn perimeter (Verdin et al., 2013). The West Fork Complex consisted of three lightning-caused wildfires, namely West Fork, Papoose and Windy Pass. Our study site is located Landsat ARD tile path/row 10/10 (see the black rectangle in Fig. 6), which covers all the burned region of Papoose fire (see Fig.9). Caused by lightning, the Papoose fire starts on June 19, 2013, spread with a southeast direction, and was considerably dampened by precipitation on July 19, 2013 (Cyphers et al., 2019; United States Department of, 2014). All Landsat ARD images between 1996 and 2019 (25 years) were downloaded for analysis. A fire perimeter map for this specific fire provided by GeoMAC mapping application (https://rmgsc.cr.usgs.gov/outgoing/GeoMAC/) was used as our reference map. Directed by United States Geological Survey (USGS), GeoMAC updates the fire perimeter data based upon inputs from incident intelligence sources, GPS data, infrared imagery from satellite platform (Walters et al., 2011), and provides the most accurate perimeter map for this fire to our best knowledge.

The second disturbance site was chosen for gypsy moth (*Lymantria dispar*) infestation in Southern New England, which covers southern Massachusetts, northeast Connecticut, and northwest Rhode Island. This is a peri-urban region with 56.7% forest cover (i.e., 34.8% hardwood, 17.8% mixed and 4.1% conifer), and 26.7% developed area and 10.8% wetlands (See Fig. 8D). This study area contains the locations that experienced from gypsy moth outbreak that started in 2015, spiked in 2017 (Pasquarella et al., 2018). Compared with fire or harvest disturbance, insect disturbances often lead to short-term or gradual spectral

457 changes (Vogelmann et al., 2016). A gypsy moth infestation can consume a large quantity of foliage and
458 sometimes causes a near-total defoliation over a season or two (Townsend et al., 2004), but often starts to
459 recover very soon for the following year, so the change signal is commonly ephemeral (Vogelmann et al.,
460 2016). In addition, infested stands typically consist of two or more dominant tree species usually
461 represented by multi-aged and multi-sized populations(Hart and Veblen, 2015), making the detection all
462 the more challenging because of mixed spectral response from various tree species. All Landsat ARD
463 images for path/row 30/6 in recent 10 years (2010-2019) were downloaded and preprocessed. The Aerial
464 Detection Survey (ADS) data[6] were used as reference dataset. The ADS data are polygon-based forest
465 health maps from visually-defined polygons for a variety of specific insects and disease, annually reported
466 by United States Department of Agriculture (USDA). It has been reported that the ADS data have high
467 omission and commission rates respectively as 32% and 33% (Johnson and Ross, 2008). The ADS data,
468 however, are a valuable source for indicating an approximate region for forest disease at a broad-scale
469 (minimum mapping unit as 5 ha) (Hart and Veblen, 2015; Preisler et al., 2012), and the timing of disease
470 occurrence.

471 # 5. Results

472 ## 5.1 Quantitative accuracy assessment

473 We tested COLD and S-CCD against a holdout validation set (n = 1891) for a series of threshold probability.
474 The omission, commission and F1 score (see annotation around markers) for each test have been shown in
475 Fig. 7A. S-CCD outperforms COLD at lower thresholds at 0.90, 0.925 and 0.95 for F1 score, while COLD
476 is slightly better at higher thresholds at 0.975 and 0.99. The best accuracy they reached are close: S-CCD
477 achieve the best performance as a F1 score of 0.793 (0.95 threshold probability, 20.1% omission and 21.4%
478 commission errors), while COLD reaches the best accuracy as F1 score of 0.789 (0.975 threshold
479 probability, 24.6% omission and 17.2% commission errors).

[6] http://www.foresthealth.fs.usda.gov/portal/Flex/IDS

We also evaluated the performance of S-CCD and COLD against seven forest disturbance categories with a threshold probability of 0.95 (Fig. 7B). Though COLD showed the best F1 score at the probability 0.975, a probability threshold of 0.95 is chosen considering: 1) to keep consistent for comparison; and 2) COLD achieved a better balance of omission and commission errors at probability 0.95. As Fig. 7B shows, S-CCD and COLD have very close omission errors for 'Harvest', 'Mechanical' and 'Wind'; S-CCD achieved lower omission error rate in the disturbance category 'Stress' (16.4% v.s. 24.6%) and 'Fire' (31.3% v.s. 35.8%), but is worse in 'Hydrology' (12.5% v.s. 37.5%) and 'Other' (32.5% v.s. 22.5%). Surprisingly, the two approaches both have relatively high omission errors for 'fire' disturbance, which is often known for causing large change magnitude from satellite images (Cohen et al., 2016). The reason is that some low-severity/underground fire cases are included in the reference dataset, which causes only subtle spectral change magnitude. The extremely low error rate for 'Wind' category is because the number of 'Wind' samples (n = 13) is small and might be underrepresented in our database. Note that per-category accuracy results of COLD for our tests are distinct with the results in Section 4.1 in (Zhu et al., 2019), which is mainly due to 1) we used a lower threshold, 0.95, instead of 0.99; 2) different choices for training and holdout reference samples due to random split; 3) only forest samples are analyzed.

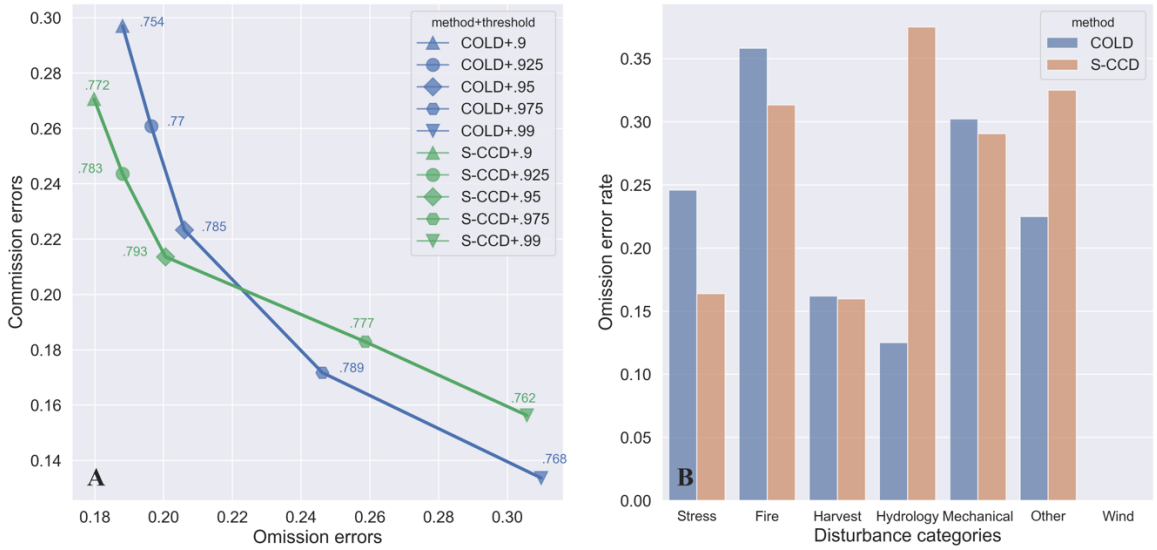

Fig. 7. Quantitative accuracy assessment results of COLD and S-CCD based on a holdout reference sample set (n = 1,891). A) shows omission, commission errors using a series of probability thresholds as 0.9, 0.925, 0.95, 0.975 and 0.99. The F1 score is used to evaluate the overall accuracy combining omission and commission errors, annotated around each marker. B) reports the omission errors of COLD and S-CCD for each disturbance category.

5.2 Qualitative accuracy assessment

For qualitative comparison, S-CCD and COLD were implemented to detect timing of forest disturbances respectively for Papoose fire and gypsy moth infestation. A consistent probability threshold as 0.95 was applied for both algorithms.

Fig. 8 shows the detection results of S-CCD and COLD for the Papoose fire site. Visually, COLD and S-CCD show very similar detection results for abrupt disturbance categories such as moderate/high-severity fire. As this region has been heavily affected by spruce beetle since 2010 (Hart and Veblen, 2015), we selected the breakpoints only detected in 2013, that is the year for Papoose fire, with an assumption that most of these breakpoints are associated with the fire, not spruce beetle attack. To assess accuracy of timings for these breakpoints, we outputted month maps for the breakpoints detected in 2013. These breakpoints mostly occurred in June and July (see Fig. 8A and B), which are well matched with the active temporal

514 window of Papoose fire on the historical records (Cyphers et al., 2019; United States Department of, 2014),
515 indicating high temporal accuracy of detected breakpoints for both methods. To further evaluate spatial
516 accuracy for damage mapping, we compare two detection maps with GeoMAC fire perimeter map (Fig.
517 8C). GeoMAC contains some commission errors for mapping fire damage areas that are actually bare land
518 from High-resolution Satellite imagery, while COLD and S-CCD both accurately labeled them as 'no-attack'
519 (see the example of Fig. 8D, E and F). It is noteworthy that Landsat 7 related scan-line corrector (SLC)
520 artifacts can be both seen in the two breakpoint month maps, where the 'month of disturbance' was labeled
521 as July, one month later than it should be. The disturbance dates detected by COLD and S-CCD may show
522 several days to a month as delayed, if the pixels happen to have data gaps right after the disturbance dates
523 due to the SLC-off issue.

524

525

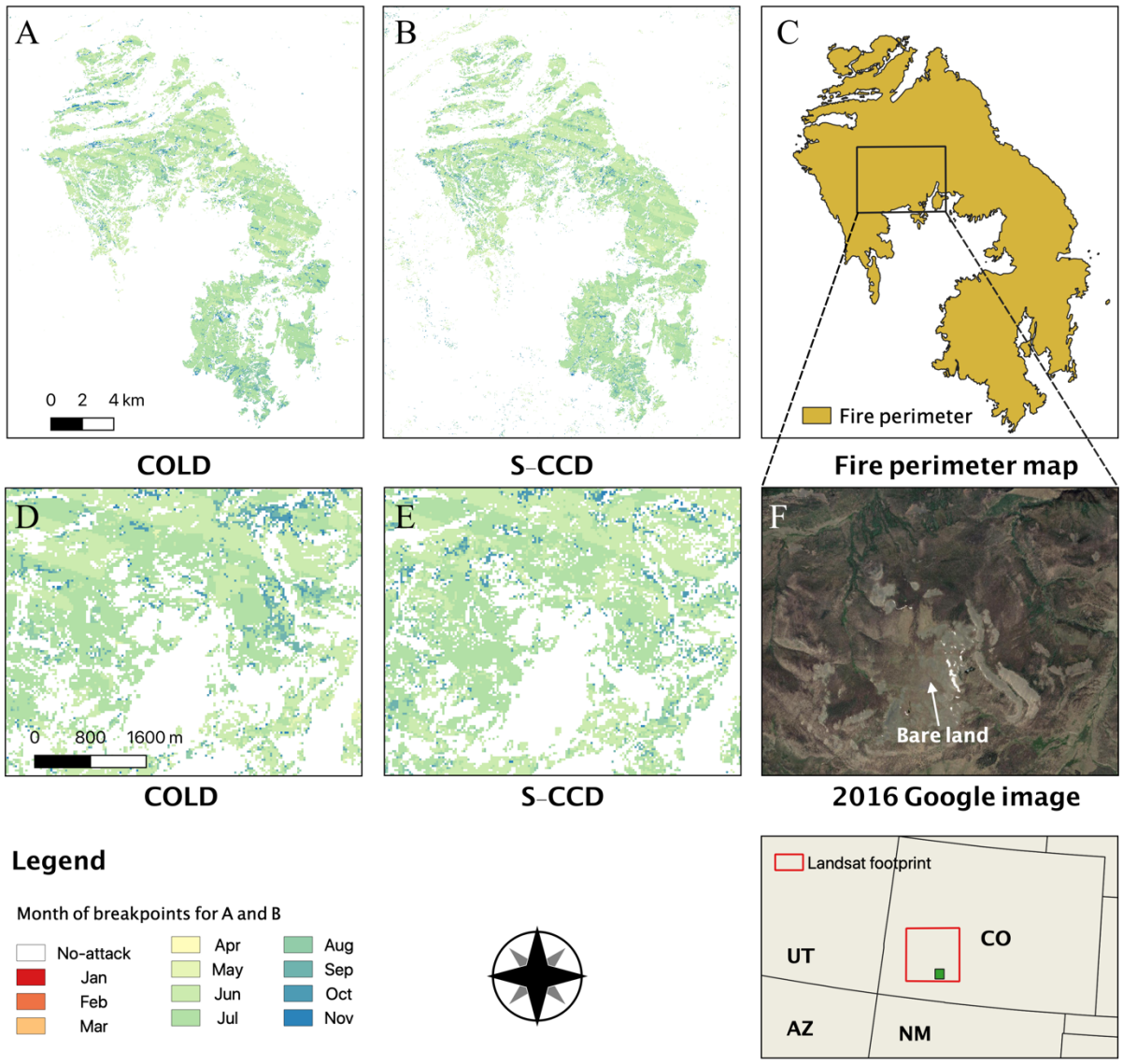

Fig. 8. Qualitative comparison for Papoose fire site (Landsat ARD 10/10) in Southeast Colorado among COLD (A), S-CCD (B) and GeoMAC fire perimeter map (C). COLD and S-CCD both use the probability threshold as 0.95. The color for A) and B) denotes the month of breakpoints detected in 2013: the spectrum ranging from red to blue corresponds to months of breakpoints from January to November; the white are no-attack regions in 2013. D), E) and F) shows an example region that COLD and S-CCD both accurately delineated non-attack bare land while GeoMAC over-detects it as fire region.

For the gypsy moth scene (Fig. 9), we compared years of breakpoints detected with Aerial Surveying Detection (ADS) data. Considering the ADS disturbance maps have the inter-mixing of several years of

insect-induced tree mortality, the reference map chose the disturbance year as the first year that a disturbance captured by the ADS. Most disturbance events detected by COLD and S-CCD are concentrated at the deciduous forest cover regions of the 2016 NLCD map (Fig. 9D). The disturbance years indicated by two algorithms matched that of the ADS data, which are primarily the year of 2016 and 2017. This finding is consistent with the historical record that a major outbreak began in early summer 2016, led by a series of unusually dry springs (2014–2016) (Pasquarella et al., 2017). Admittedly, both algorithms yield much fewer affected regions than that the ADS shows. Considering that Pasquarella et al. (2017) got the same result for their study in the Southern New England region, those omission errors might be due to overestimation of tree mortality regions in aerial sketch mapping. For comparative analysis, we found that COLD missed some regions affected by gypsy moth (e.g., the dashed blue circle in Fig. 9A), while S-CCD found most parts of the same region as forest disturbance. The general locations and the disturbance years for extra regions detected by S-CCD have agreement with the ADS data (see the dashed circle in Fig.9C), proving that these extra breakpoints detected by S-CCD for this region are related to forest damage caused by gypsy moth. In addition, the damaged trees, which appears to be ‘gray’ color, can be clearly identified from 2018 high-resolution Google satellite image (see Fig. 9G), and the geometric shape of damaged area in the high-resolution imagery align with that of the disturbance region detected by S-CCD (Fig. 9F).

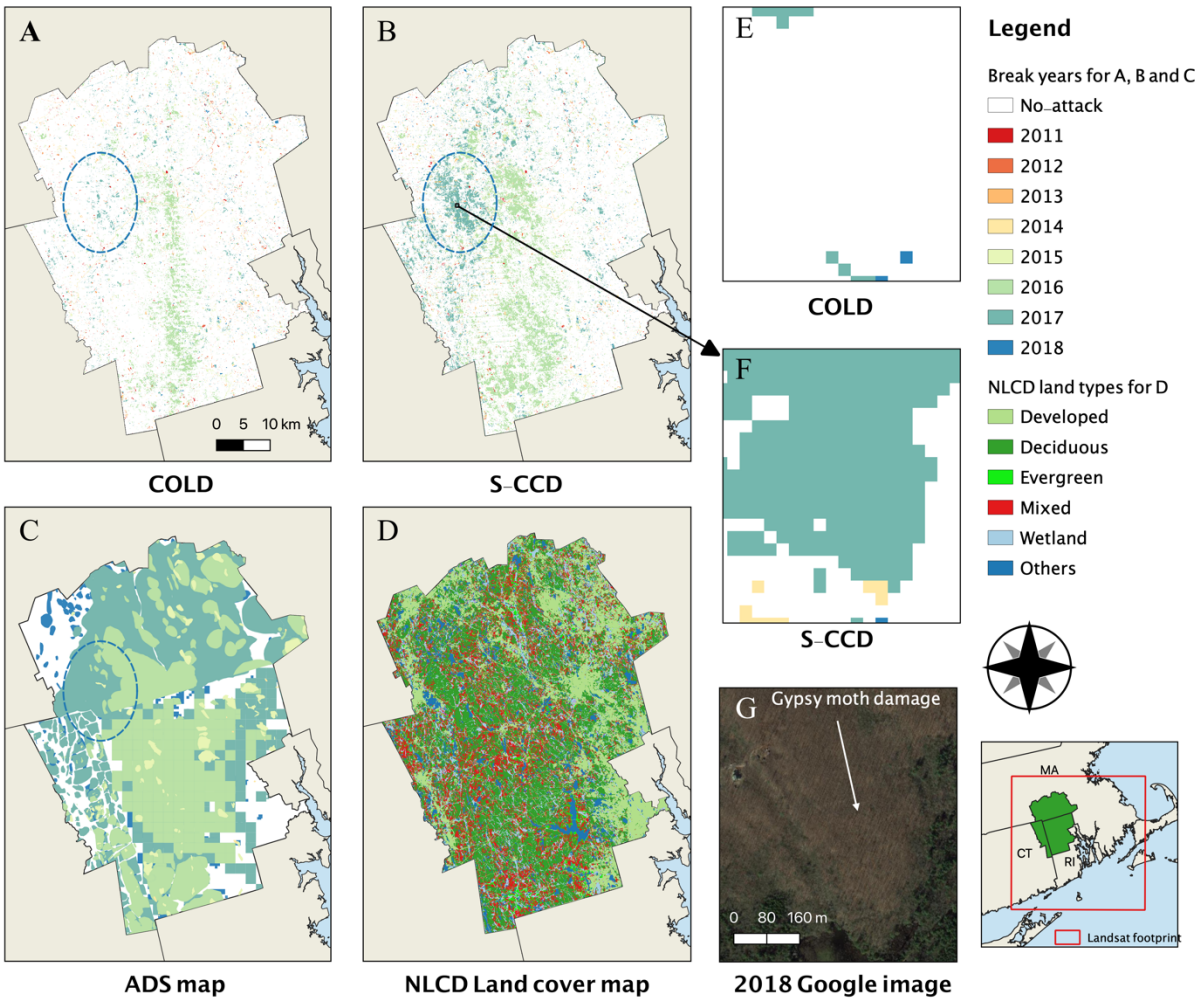

Fig. 9. Qualitative comparison for gypsy moth site (Landsat ARD 30/6) in Southern New England among COLD (A), S-CCD (B) and the ADS reference map (C). (D) shows the land cover types from NLCD 2016. COLD and S-CCD both use the probability threshold as 0.95. The color for (A), (B) and (C) denote the disturbance year indicated by each data source: the spectrum ranging from red to blue corresponds to the years from 2011 to 2018. Fig.9 E), F) and G) shows an example region that COLD missed gypsy moth damage which can be clearly identified in the high-resolution Google imagery.

5.3 Efficiency test and software implementation

We implemented COLD and S-CCD in the high-performance C programming language. The C package named 'S-CCD' is downloadable from https://github.com/SuYe99/s-ccd (the repo was temporally set to be private for now, and the package was sent into 'supplementary materials' for the review process). A Python

566 interface is also provided by the package. The software implemented a shared memory parallelization for
567 COLD and S-CCD under a Linux/MacOS desktop environment, and can be easily adapted for a High-
568 Performance Computing (HPC) environment. It is noteworthy that our C-based COLD has been 15-20
569 times faster than the original MATLAB-based implementation.

570 To test the efficiency for C-based COLD and S-CCD, we used a 'dummy' Landsat ARD scanline which is
571 a standard sample set of 5,000 pixel-based time series plots selected from our reference sample set. The
572 sample set consists of 3,782 forest plots and 1,218 non-forest plots. To uncover the effects of monitoring
573 span on the speed, we pruned each time series into three different lengths of time series records, that is 10
574 years (2008-2017), 20 years (1998-2017) and 34 years (1984-2017). The results are summarized in Fig.
575 10. S-CCD can achieve up to ~4.4 times faster than the C-based COLD (with 34-year time series records).
576 With the length of records decreasing, the efficiency improvement of S-CCD over COLD declines, as ~3.5
577 times at 20-year time series records, and ~1.8 time faster at 10-year time series records. This is because S-
578 CCD improves efficiency mainly at the step of the model update; a longer time series needs a greater
579 number for model updates to complete a detection, and hence more significant efficiency improvement
580 made by S-CCD. For a standard 20-year Landsat ARD time series, our S-CCD program takes only ~6
581 minutes to finish a detection for a 5000-pixel scanline, and ~500 computing hours for a Landsat ARD scene.

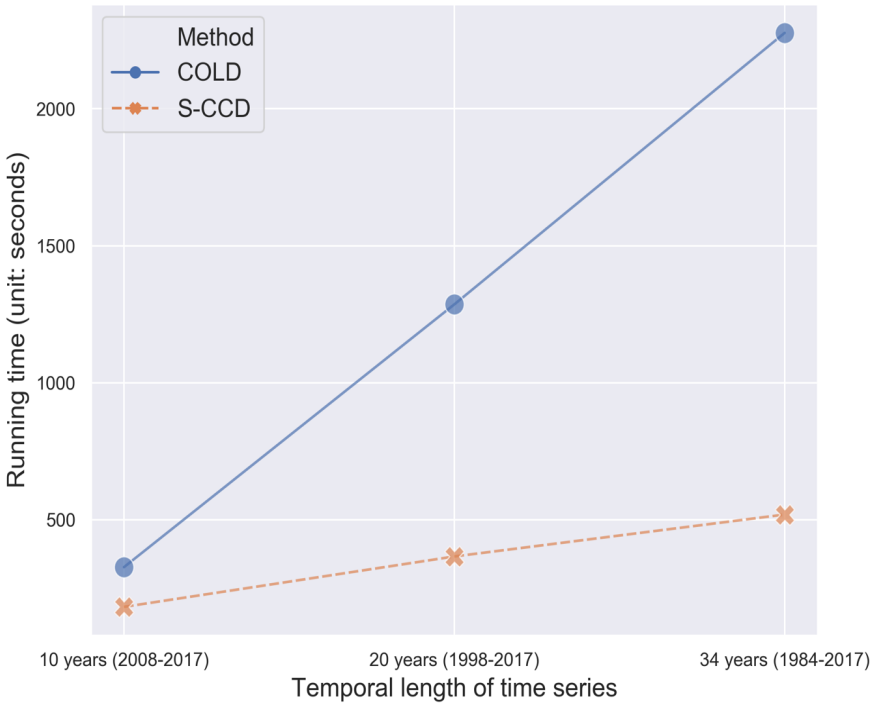

582

583 **Fig. 10. The result for the efficiency test based on a dummy Landsat ARD scanline (5,000 sample**
584 **pixels). Each time series are pruned as three versions for time series records, that is 10 years (2008-**
585 **2017), 20 years (1998-2017), 34 years (1984-2017). The result shows that the efficiency of S-CCD**
586 **was increased as the length of time series increased, and can be up to 4.4 times faster than COLD.**
587 **The CPU is Intel(R) Core (TM) i7-4790, 3.60GHz.**
588

589 ## 6. Discussion

590 The quantitative accuracy assessment indicates that the differences between the best accuracy achieved by
591 S-CCD and COLD are only 0.4% (see Fig. 7A, 0.793 v.s. 0.789). The primary reason is that our plot
592 database is generated from random sampling over a nation-wide region, for which 63% of the forest
593 disturbances are harvesting activities; the two approaches have very similar performance for detecting
594 strong spectral signals yielded by those disturbances with medium- or high-severity and homogeneous tree
595 damages such as harvest disturbances (omission errors: 16% v.s. 16.2%). Our map-based evaluation for
596 Papoose fire case can confirm this conclusion.

We noticed that, however, S-CCD achieved noticeably less omission errors than COLD for those lower-magnitude disturbances such as drought stress and low-severity fire (see Fig. 7b). This finding was confirmed by our qualitative comparison for the case study of gypsy moths. The reason is three-fold. First, S-CCD allows for known changes in the structure of the system over time, and often can achieve a better model fitting than COLD that assumes the rigidity of "linear trend + harmonic cycles". We calculated the average RMSE for each band using all our 3,782 samples. The results, as shown in Table 1, indicate that S-CCD has generally lower average RMSE than COLD for all seven spectral bands other than NIR and thermal bands (thermal band is not used to compute change magnitudes for both approaches, and thereby has no effects on break detection). As the two approaches both evaluated change magnitude relative to the RMSE, the lower RMSE means that S-CCD model is more sensitive to those low-magnitude spectral changes.

Table 1: the average RMSE of COLD and S-CCD for each band using 3,782 forest samples across the conterminous United States (the bold columns are the two bands that S-CCD has higher RMSE than COLD)

Band	Blue	Green	Red	**NIR**	SWIR1	SWIR2	**Thermal**
COLD	122.682	117.127	122.473	**273.336**	197.937	151.032	**389.227**
S-CCD	119.061	110.761	118.476	**279.478**	191.518	150.098	**401.061**

Second, S-CCD uses a new temporally-adjusted peek window, for which the window width is defined as calendar days, not a fixed observation number. Fig.11 is an example of NIR-based time series from our gypsy moth case: S-CCD successfully detected the gypsy moth attack with a breakpoint as '2016-05-17' (the black solid line in Fig. 11B) while missed by the COLD. COLD employs a fixed number of 12 observations for its peak window as the median revisit days is 8 days for this case (see Formula S2 in the supplementary material of (Zhu et al., 2019)). If the peek window spans over a period of sparse clear observation such as May and June on 2016, the peek window has to be extended to later months in order to include enough clear observations. Differently, S-CCD defines the peek window as the minimum width of

80 calendar days, so when the monitoring stands at '2016-05-17' (the breakpoint detected), the peek window of S-CCD stops at the date '2016-07-20' (see the red dashed line in Fig. 11B), roughly one month earlier than that of COLD ('2016-08-21', see the red dashed line in Fig. 11A). A gradual decrease in NIR band ('greendown') is commonly observed during the later summer in deciduous broadleaf forests (Elmore et al., 2012; Melaas et al., 2013), which is also shown in the harmonic modeling curve of Fig 11A. As a result, the damage signal was overridden by normal phenological changes at the end of the peek window for COLD, causing the breakpoint to be missed for detection.

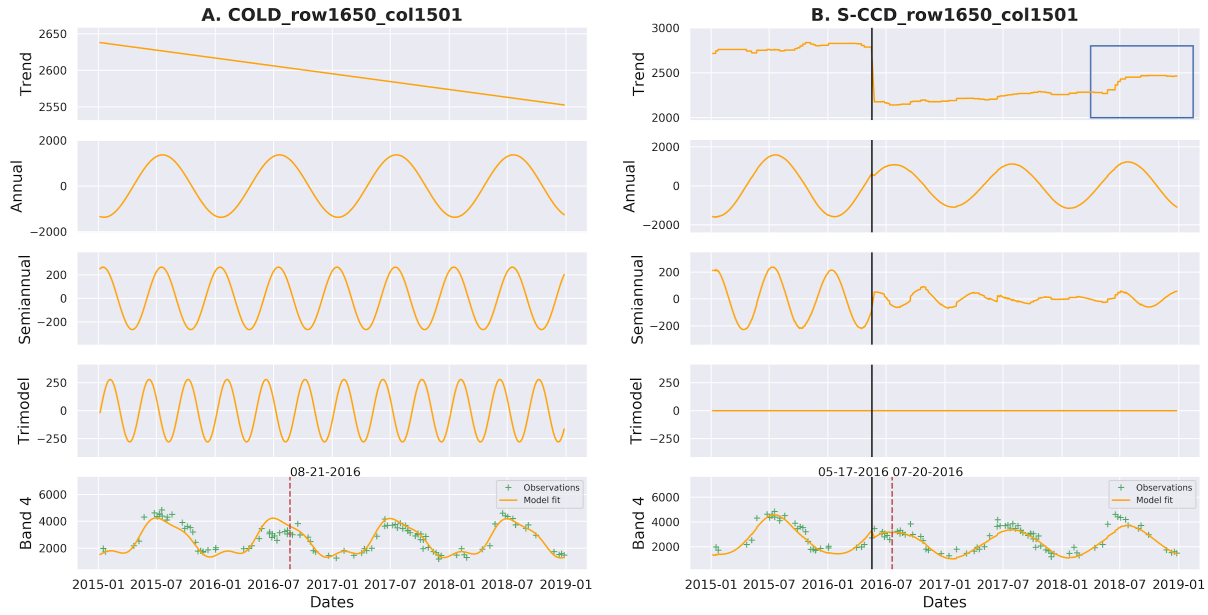

Fig. 11. An example where S-CCD detects the breakpoint that was missed by COLD, from a gypsy moth attack site. The black line: the breakpoint detected. The red dashed lines: the ending dates of the peek window for each method, when the monitoring stands at '05-17-2016' (the peak window of S-CCD is finished with one month earlier than COLD). The blue rectangle shows the recent signal for increasing NIR associated with forest regeneration, which is revealed by 'trend' component of S-CCD (The trimodel component is set as a constant '0' for S-CCD here because the trimodel component has been excluded for S-CCD).

Third, if COLD/CCDC misses observations at the beginning of a gradual change, the algorithm will incorporate these 'change' observations to refit the model with a slight slope associated with 'degradation'. This slope results in lower change magnitudes for subsequent observations, possibly causing a complete

missing detection for the break (Bullock et al., 2019). Owing to no slope component in our predefined structure (see Equation 6), S-CCD, however, assumes that the trend state to be constant for future, rather than continue degrading, thereby owns a chance to detect the breakpoint later.

S-CCD also provides a rich set of information for help elucidate short-term fluctuations via its continuous varying expression for trend and seasonality. For the example of Fig.11, the NIR trend component for S-CCD appears to be increasing after the year 2018 (see the blue rectangle in Fig.11B), indicating the greenness is recovering. COLD fails to unveil these subtle signals because it generalizes linear trend and seasonality using a simple harmonic model. S-CCD is more informative for probing such-like short-term and subtle signals which might have important ecological implications, owing to its ability to model more complex nonlinear temporal dynamics. It is worth mentioning that our software package provides this functionality of visualization for plotting dynamics of each state.

Another obvious advantage of S-CCD is that it is a completely online monitoring algorithm, which can be directly used for near real-time forest monitoring. S-CCD improves several steps of COLD and enables a continuous monitoring in a completely recursive form, such as the adjusted peek window, recursive temporal RMSE. More importantly, the core technique for S-CCD, the Kalman filter, is a powerful real-time algorithm well known for its high computational efficiency and short-memory requirement. For COLD, limited by its manner for re-constructing the model per observation, it requires reading all images into the system to rebuild harmonic curves for each new observation. Instead, S-CCD just needs to update those parameter files (e.g., states and covariance) once the initialization is finished, which can reduce ~ 95% of data inputs for monitoring each new observation. In addition, the Kalman filter has an extremely simple mathematical treatment for dealing with missing data, therefore is an ideal tool for processing remote sensing time series which often have irregular temporal intervals between successive observations.

A possible concern is that S-CCD assumes a consistent structure of time series for trend, annual and semi-annual harmonic items (equal to 6-coefficient harmonic models), while Zhu et al. (2019) suggested using a harmonic model with a maximum coefficient as 8, including trend, annual, semi-annual and trimodal

harmonic items (frequency = ⅓ year). As such, we tested adding an additional trimodal cycle component into the presumed time series structure of S-CCD, and found that the best F1 score decreased from 0.795 to 0.706 for S-CCD (see Fig. S4 in the supplementary material). In a harmonic regression, trimodal component can be viewed as an additional modifier to annual and semi-annual curves (Eastman et al., 2009). The state space model adopted a totally different strategy to resolve unexplained variance from annual and semi-annual curves: the state space model assumes that the trend and seasonality states are evolving as time goes by (see Fig. 2B), instead of following a fixed set of harmonic coefficients, thus the unexplained variances can be 'ingested' immediately by changes in structure over time. Another reason might be that we focus on forest disturbance detection for this study, while the trimodal component is often found to be more useful for modeling cropland dynamics.

Admittedly, COLD is designed for detecting/characterizing all types of land disturbances, not limited to forest disturbances. We tested S-CCD against a reference dataset for comprehensive land types, and got a slightly lower F1 score compared with COLD (0.69 vs 0.71). Our test shows that S-CCD performs less ideal under a highly-fluctuated environment, and is more prone to over-detection due to those ephemeral changes that have a high change magnitude, such as moisture change for grassland/bare land and agricultural rotation. To alleviate this issue, our software package enables users to specify a mask for focused study area, which can exclude the regions where uninterested land change occur and greatly improve processing efficiency as well. Yet, there is still much studies that is needed to analyze characteristics of detected breaks and select breaks only linked to targeted physical processes. Another reason for the unsatisfactory results is that we often have multiple historical data sources to confirm forest disturbances such as the ADS and the LANDFIRE products, but reliable references for the other non-forest land disturbance are lacking. The quality of our non-forest land samples might affect the final accuracy result. Our future work will be directed into 1) modifying S-CCD to accommodate other applications such as agricultural shifts and urban expansion, and 2) tuning the algorithm for the optimal parameters, such as

probability threshold and *min_peek_days*, for better detection of targeted change agents and timely warning of land disturbance.

7. Conclusion

We presented an improved time series framework, Stochastic Continuous Change Detection (S-CCD), for near real-time forest disturbance monitoring. The new approach introduces the state space model into the current framework for Continuous Monitoring of Land Disturbance (COLD), to facilitate a complete near real-time analytics of forest dynamics and improve computational efficiency. S-CCD provides an accurate mapping for timing and change magnitude of forest disturbance, and uncovers complex nonlinear dynamics from time series data. Especially S-CCD can improve the monitoring for those disturbances that induce subtle spectral changes.

Acknowledgement

This work has been supported with funding from American Society of Photogrammetry and Remote Sensing (ASPRS) William A. Fisher Scholarship and Albert, and Norma and Howard Geller ’77 Endowed Research Awards to Su Ye. We also gratefully acknowledge the support of USGS-NASA Landsat Science Team (LST) Program for Toward Near Real-time Monitoring and Characterization of Land Surface Change for the Conterminous US (140G0119C0008) to Zhe Zhu.

Appendix

The system matrices for 'trend+annual+semi-annual' time series structural model are defined by

$$Z = (1, 1, 0, 1, 0) \quad \text{(A1)}$$

$$Q = diag(\sigma_\xi^2,\ \sigma_{\omega,annual}^2,\ \sigma_{\omega^*,annual}^2,\ \sigma_{\omega,semi}^2,\ \sigma_{\omega^*,semi}^2) \quad \text{(A2)}$$

$$T = \begin{bmatrix} 1 & 0 & 0 & 0 & 0 \\ 0 & \cos\left(\frac{2\pi}{365.25}\right) & \sin\left(\frac{2\pi}{365.25}\right) & 0 & 0 \\ 0 & -\sin\left(\frac{2\pi}{365.25}\right) & \cos\left(\frac{2\pi}{365.25}\right) & 0 & 0 \\ 0 & 0 & 0 & \cos\left(\frac{2\pi}{2*365.25}\right) & \sin\left(\frac{2\pi}{2*365.25}\right) \\ 0 & 0 & 0 & -\sin\left(\frac{2\pi}{2*365.25}\right) & \cos\left(\frac{2\pi}{2*365.25}\right) \end{bmatrix} \quad \text{(A3)}$$

The Kalman filter recursion for the general Gaussian model of form are

$$v_{t,i} = y_{t,i} - Z\, a_{t,i} \quad \text{(A4)}$$

$$F_{t,i} = Z\, P_{t,i} Z^T + H_i \quad \text{(A5)}$$

$$K_{t,i} = P_{t,i} Z^T \quad \text{(A6)}$$

$$a_{t|t,i} = a_{t,i} + K_{t,i} F_{t,i}^{-1} v_{t,i} \quad \text{(A7)}$$

$$a_{t+1,i} = T\, a_{t|t,i} \quad \text{(A8)}$$

$$P_{t+1,i} = T\left(P_{t,i} - K_{t,i} K_{t,i}^T F_{t,i}^{-1}\right) T^T + Q_i \quad \text{(A9)}$$

Where

$y_{t,i}$: the observation at time t for band i

$v_{t,i}$: the innovation, namely the difference between predicted and actual observations, at time t for band i

Z: the system matrix that determines which items in the state vector are included for the observation

$K_{t,i}$: the Kalman gain which is the relative ratio of being assigned to the model update is from the innovation at time t for band i

$P_{t,i}$: the covariance matrix at time t for band i

$a_{t|t,i}$: the filtered states at time t for band i

$F_{t,i}$: the variance of the innovation $v_{t,i}$

Q_i: the process noise for band i

H_i: the observational noise for band i

For missing observation, there is no innovation $v_{t,i}$. Therefore, the mathematical treatment for state and covariance matrix updates can be simply put as

$$a_{t+1,i} = T\, a_{t|t,i} \quad \text{(A10)}$$

$$P_{t+1,i} = T P_{t,i} T^T + Q_i \quad \text{(A11)}$$

Reference

Allen, C.D., Breshears, D.D., & McDowell, N.G. (2015). On underestimation of global vulnerability to tree mortality and forest die-off from hotter drought in the Anthropocene. *Ecosphere, 6*, 1-55

Brockwell, P.J., & Davis, R.A. (2013). *Introduction to Time Series and Forecasting*. Springer Science & Business Media

Brown, J.F., Tollerud, H.J., Barber, C.P., Zhou, Q., Dwyer, J.L., Vogelmann, J.E., Loveland, T.R., Woodcock, C.E., Stehman, S.V., Zhu, Z., Pengra, B.W., Smith, K., Horton, J.A., Xian, G., Auch, R.F., Sohl, T.L., Sayler, K.L., Gallant, A.L., Zelenak, D., Reker, R.R., & Rover, J. (2019). Lessons learned implementing an operational continuous United States national land change monitoring capability: The Land Change Monitoring, Assessment, and Projection (LCMAP) approach. *Remote Sensing of Environment*, 111356

Bullock, E.L., Woodcock, C.E., & Holden, C.E. (2019). Improved change monitoring using an ensemble of time series algorithms. *Remote Sensing of Environment*, 111165

Burkett, V.R., Wilcox, D.A., Stottlemyer, R., Barrow, W., Fagre, D., Baron, J., Price, J., Nielsen, J.L., Allen, C.D., Peterson, D.L., Ruggerone, G., & Doyle, T. (2005). Nonlinear dynamics in ecosystem response to climatic change: Case studies and policy implications. *Ecological Complexity, 2*, 357-394

Carlson, A.R., Sibold, J.S., Assal, T.J., & Negrón, J.F. (2017). Evidence of compounded disturbance effects on vegetation recovery following high-severity wildfire and spruce beetle outbreak. *PLoS ONE, 12*, e0181778

Claverie, M., Vermote, E.F., Franch, B., & Masek, J.G. (2015). Evaluation of the Landsat-5 TM and Landsat-7 ETM+ surface reflectance products. *Remote Sensing of Environment, 169*, 390-403

Cohen, W.B., Healey, S.P., Yang, Z., Stehman, S.V., Brewer, C.K., Brooks, E.B., Gorelick, N., Huang, C., Hughes, M.J., & Kennedy, R.E. (2017). How Similar Are Forest Disturbance Maps Derived from Different Landsat Time Series Algorithms? *Forests, 8*, 98

Cohen, W.B., Yang, Z., Stehman, S.V., Schroeder, T.A., Bell, D.M., Masek, J.G., Huang, C., & Meigs, G.W. (2016). Forest disturbance across the conterminous United States from 1985–2012: The emerging dominance of forest decline. *Forest ecology and management, 360*, 242-252

Curran, L.M., & Trigg, S.N. (2006). Sustainability science from space: quantifying forest disturbance and land-use dynamics in the Amazon. *Proceedings of the National Academy of Sciences of the United States of America, 103*, 12663-12664

Cyphers, L., Mackes, K., & Duda, K. (2019). Timber Losses from West Fork Complex Fire in Southwest Colorado. *For. Prod. J.*

Dale, V.H., Joyce, L.A., McNulty, S., Neilson, R.P., Ayres, M.P., Flannigan, M.D., Hanson, P.J., Irland, L.C., Lugo, A.E., & Peterson, C.J. (2001). Climate change and forest disturbances. *BioScience, 51*, 723-734

Davis, M.H.A., & Vinter, R.B. (1985). Stochastic models. *Stochastic Modelling and Control*, 60-99

Durbin, J., & Koopman, S.J. (2012). *Time Series Analysis by State Space Methods: Second Edition*. OUP Oxford

Dwyer, J., Roy, D., Sauer, B., Jenkerson, C., Zhang, H., & Lymburner, L. (2018). Analysis Ready Data: Enabling Analysis of the Landsat Archive. *Remote Sensing, 10*

Eastman, J.R., Sangermano, F., Ghimire, B., Zhu, H., Chen, H., Neeti, N., Cai, Y., Machado, E.A., & Crema, S.C. (2009). Seasonal trend analysis of image time series. *International journal of remote sensing, 30*, 2721-2726

Eastman, J.R., Sangermano, F., Machado, E.A., Rogan, J., & Anyamba, A. (2013). Global trends in seasonality of normalized difference vegetation index (NDVI), 1982–2011. *Remote Sensing, 5*, 4799-4818

Elmore, A.J., Guinn, S.M., Minsley, B.J., & Richardson, A.D. (2012). Landscape controls on the timing of spring, autumn, and growing season length in mid-Atlantic forests. *Global change biology, 18*, 656-674

Hart, S.J., & Veblen, T.T. (2015). Detection of spruce beetle-induced tree mortality using high-and medium-resolution remotely sensed imagery. *Remote Sensing of Environment, 168*, 134-145

Helske, J. (2016). KFAS: Exponential Family State Space Models in R. *arXiv [stat.CO]*

Jamali, S., Jönsson, P., Eklundh, L., Ardö, J., & Seaquist, J. (2015). Detecting changes in vegetation trends using time series segmentation. *Remote Sens. Environ., 156*, 182-195

Johnson, E.W., & Ross, J. (2008). Quantifying error in aerial survey data. *Australian Forestry, 71*, 216-222

Ju, J., Roy, D.P., Vermote, E., Masek, J., & Kovalskyy, V. (2012). Continental-scale validation of MODIS-based and LEDAPS Landsat ETM+ atmospheric correction methods. *Remote Sensing of Environment, 122*, 175-184

Kalman, R.E. (1960). A new approach to linear filtering and prediction problems. *Int. J. Eng. Trans. A, 82*, 35-45

Kautz, M., Meddens, A.J., Hall, R.J., & Arneth, A. (2017). Biotic disturbances in Northern Hemisphere forests–a synthesis of recent data, uncertainties and implications for forest monitoring and modelling. *Global Ecology and Biogeography, 26*, 533-552

Kennedy, R.E., Andréfouët, S., Cohen, W.B., Gómez, C., Griffiths, P., Hais, M., Healey, S.P., Helmer, E.H., Hostert, P., Lyons, M.B., & Others (2014). Bringing an ecological view of change to Landsat-based remote sensing. *Front. Ecol. Environ., 12*, 339-346

Kennedy, R.E., Yang, Z., & Cohen, W.B. (2010). Detecting trends in forest disturbance and recovery using yearly Landsat time series: 1. LandTrendr—Temporal segmentation algorithms. *Remote Sensing of Environment, 114*, 2897-2910

Masek, J.G., Goward, S.N., Kennedy, R.E., Cohen, W.B., Moisen, G.G., Schleeweis, K., & Huang, C. (2013). United States Forest Disturbance Trends Observed Using Landsat Time Series. *Ecosystems, 16*, 1087-1104

Masek, J.G., Huang, C., Wolfe, R., Cohen, W., Hall, F., Kutler, J., & Nelson, P. (2008). North American forest disturbance mapped from a decadal Landsat record. *Remote Sensing of Environment, 112*, 2914-2926

Melaas, E.K., Friedl, M.A., & Zhu, Z. (2013). Detecting interannual variation in deciduous broadleaf forest phenology using Landsat TM/ETM+ data. *Remote Sensing of Environment, 132*, 176-185

Olsson, P.-O., Lindström, J., & Eklundh, L. (2016). Near real-time monitoring of insect induced defoliation in subalpine birch forests with MODIS derived NDVI. *Remote Sensing of Environment, 181*, 42-53

Paritsis, J., & Veblen, T.T. (2011). Dendroecological analysis of defoliator outbreaks on Nothofagus pumilio and their relation to climate variability in the Patagonian Andes. *Global change biology, 17*, 239-253

Pasquarella, V., Bradley, B., & Woodcock, C. (2017). Near-Real-Time Monitoring of Insect Defoliation Using Landsat Time Series. *Forests, 8*, 275

Pasquarella, V., Elkinton, J.S., & Bradley, B.A. (2018). Extensive gypsy moth defoliation in Southern New England characterized using Landsat satellite observations. *Biol. Invasions, 20*, 3047-3053

Pasricha, G.K. (2006). Kalman Filter and its Economic Applications

Pechony, O., & Shindell, D.T. (2010). Driving forces of global wildfires over the past millennium and the forthcoming century. *Proceedings of the National Academy of Sciences, 107*, 19167-19170

Preisler, H.K., Hicke, J.A., Ager, A.A., & Hayes, J.L. (2012). Climate and weather influences on spatial temporal patterns of mountain pine beetle populations in Washington and Oregon. *Ecology, 93*, 2421-2434

Rogan, J., & Mietkiewicz, N. (2015). Land cover change detection. *Land Resources Monitoring, Modeling, and Mapping with Remote Sensing; Thenkabail, PS, Ed*, 579-603

Schmidt, S.F. (1981). The Kalman filter - Its recognition and development for aerospace applications. *J. Guid. Control Dyn., 4*, 4-7

Sedano, F., Kempeneers, P., & Hurtt, G. (2014). A Kalman Filter-Based Method to Generate Continuous Time Series of Medium-Resolution NDVI Images. *Remote Sensing, 6*, 12381-12408

Seidl, R., Thom, D., Kautz, M., Martin-Benito, D., Peltoniemi, M., Vacchiano, G., Wild, J., Ascoli, D., Petr, M., & Honkaniemi, J. (2017). Forest disturbances under climate change. *Nature climate change, 7*, 395-402

Townsend, P.A., Eshleman, K.N., & others (2004). Remote sensing of gypsy moth defoliation to assess variations in stream nitrogen concentrations. *Ecological*

Turner, M.G., Baker, W.L., Peterson, C.J., & Peet, R.K. (1998). Factors influencing succession: lessons from large, infrequent natural disturbances. *Ecosystems, 1*, 511-523

United States Department of, A. (2014). West Fork Fire Complex

Verbesselt, J., Hyndman, R., Newnham, G., & Culvenor, D. (2010a). Detecting trend and seasonal changes in satellite image time series. *Remote Sensing of Environment, 114*, 106-115

Verbesselt, J., Hyndman, R., Zeileis, A., & Culvenor, D. (2010b). Phenological change detection while accounting for abrupt and gradual trends in satellite image time series. *Remote Sensing of Environment, 114*, 2970-2980

Verbesselt, J., Zeileis, A., & Herold, M. (2012). Near real-time disturbance detection using satellite image time series. *Remote Sensing of Environment, 123*, 98-108

Verdin, K.L., Dupree, J.A., & Stevens, M.R. (2013). *Postwildfire debris-flow hazard assessment of the area burned by the 2013 West Fork Fire Complex, southwestern Colorado*. US Department of the Interior, US Geological Survey

Vicente-Guijalba, F., Martinez-Marin, T., & Lopez-Sanchez, J.M. (2014). Crop Phenology Estimation Using a Multitemporal Model and a Kalman Filtering Strategy. *IEEE Geoscience and Remote Sensing Letters, 11*, 1081-1085

Vogelmann, J.E., Gallant, A.L., Shi, H., & Zhu, Z. (2016). Perspectives on monitoring gradual change across the continuity of Landsat sensors using time-series data. *Remote Sensing of Environment, 185*, 258-270

Walters, S.P., Schneider, N.J., & Guthrie, J.D. (2011). Geospatial Multi-Agency Coordination (GeoMAC) wildland fire perimeters, 2008. *Data Series*

Westerling, A.L. (2016). Increasing western US forest wildfire activity: sensitivity to changes in the timing of spring. *Phil. Trans. R. Soc. B, 371*, 20150178

Woodcock, C.E., Allen, R., Anderson, M., Belward, A., Bindschadler, R., Cohen, W., Gao, F., Goward, S.N., Helder, D., & Helmer, E. (2008). Free access to Landsat imagery. *Science, 320*, 1011-1011

Ye, S., Rogan, J., & Sangermano, F. (2018). Monitoring rubber plantation expansion using Landsat data time series and a Shapelet-based approach. *ISPRS J. Photogramm. Remote Sens., 136*, 134-143

Zhao, K., Wulder, M.A., Hu, T., Bright, R., Wu, Q., Qin, H., Li, Y., Toman, E., Mallick, B., Zhang, X., & Brown, M. (2019). Detecting change-point, trend, and seasonality in satellite time series data to track abrupt changes and nonlinear dynamics: A Bayesian ensemble algorithm. *Remote Sens. Environ., 232*, 111181

Zhu, Z. (2017). Change detection using landsat time series: A review of frequencies, preprocessing, algorithms, and applications. *ISPRS Journal of Photogrammetry and Remote Sensing, 130*, 370-384

Zhu, Z. (2019). Science of Landsat Analysis Ready Data. *Remote Sensing, 11*, 2166

Zhu, Z., & Woodcock, C.E. (2012). Object-based cloud and cloud shadow detection in Landsat imagery. *Remote Sensing of Environment, 118*, 83-94

Zhu, Z., & Woodcock, C.E. (2014a). Automated cloud, cloud shadow, and snow detection in multitemporal Landsat data: An algorithm designed specifically for monitoring land cover change. *Remote Sensing of Environment, 152*, 217-234

Zhu, Z., & Woodcock, C.E. (2014b). Continuous change detection and classification of land cover using all available Landsat data. *Remote Sensing of Environment, 144*, 152-171

Zhu, Z., Woodcock, C.E., Holden, C., & Yang, Z. (2015). Generating synthetic Landsat images based on all available Landsat data: Predicting Landsat surface reflectance at any given time. *Remote Sensing of Environment, 162*, 67-83

Zhu, Z., Woodcock, C.E., & Olofsson, P. (2012). Continuous monitoring of forest disturbance using all available Landsat imagery. *Remote Sensing of Environment, 122*, 75-91

Zhu, Z., Zhang, J., Yang, Z., Aljaddani, A.H., Cohen, W.B., Qiu, S., & Zhou, C. (2019). Continuous monitoring of land disturbance based on Landsat time series. *Remote Sensing of Environment*